

# Understanding and Hinderion Ion Migration in Er,Yb:LiLuF<sub>4</sub> Core-Shell Nanoparticles for Nanothermometers with Enhanced Photoluminescence

*Mirijam Lederer<sup>a</sup>, Hannes Rijckaert<sup>b</sup> Anna M. Kaczmarek<sup>a\*</sup>*

<sup>a</sup> NanoSensing Group, Department of Chemistry, Ghent University, Krijgslaan 281- S3, B-9000 Ghent, Belgium

<sup>b</sup> SCRiPTS, Department of Chemistry, Ghent University, Krijgslaan 281- S3, B-9000 Ghent, Belgium

Email-address: [anna.kaczmarek@ugent.be](mailto:anna.kaczmarek@ugent.be)

KEYWORDS: *core-shell structures, lanthanide nanothermometers, ion migration, nanoparticles, upconversion*

## ABSTRACT

Developing core-shell nanoparticles is a common approach to improve the luminescence performance of nanomaterials, as an inert shell shields the core, which is doped with luminescent ions, from the quenching influence of the environment. Core-only nanoparticles are susceptible to solvent overtones, which can couple with the emissive dopants on the surface and quench their intensity. This is undeniably highly undesired for any luminescence application. It was recently shown by some of us that previously unreported ion migration takes place in 2%Er,18%Yb:LiLuF<sub>4</sub>@LiLuF<sub>4</sub> core-shell nanoparticles, which was proven both with energy-dispersive X-ray (EDX) maps and high temperature luminescence measurements. These findings lead us to the investigation presented here, which explores in detail how to hinder the migration of Er<sup>3+</sup> and Yb<sup>3+</sup> ions in LiLuF<sub>4</sub> and LiYF<sub>4</sub> hosts by implementing an interface region. First, different synthesis routes were explored to see if the chosen approach had any effect on the ion migration process from the doped core into the inert shell in a homogenous core-shell system. Next, a LiYF<sub>4</sub> inert shell was grown around a 2%Er,18%Yb:LiLuF<sub>4</sub> core forming a heterogenous core-shell system. We observed that the heterogeneous 2%Er,18%Yb:LiLuF<sub>4</sub>@LiYF<sub>4</sub> and LiLuF<sub>4</sub>@2%Er,18%Yb:LiYF<sub>4</sub> core-shell combinations showed significantly less ion migration based on EDX maps and high temperature luminescence measurements exhibiting behavior similar to the well-studied 2%Er,18%Yb:NaYF<sub>4</sub>@NaYF<sub>4</sub> core-shell structures which according to previous studies show no or very little ion migration.

## Introduction

Nanothermometry is a fast-developing field of research due to the possibility of remote, precise, reliable, and non-invasive temperature sensing in real time.<sup>1-4</sup> Different types of materials and read-out methods can be utilized for nanothermometry. Currently, an often-proposed novel read-out method is ratiometric thermometry.<sup>5,6</sup> Among some the most studied materials suitable for luminescence thermometry are Ln<sup>3+</sup>-based nanoparticles (NPs). Nanothermometry based on lanthanide-doped NPs commonly involves the changing ratio of the luminescence intensity of thermally coupled emission bands of one or more Ln<sup>3+</sup> ion(s). The change of the emission band ratio with increasing or decreasing temperature can be utilized to determine the temperature and its distribution. Various host materials have been reported in literature and the materials are most commonly doped with a two Ln<sup>3+</sup>-ion system, such as the combination of Er<sup>3+</sup> and Yb<sup>3+</sup>.<sup>5,6</sup> Nanothermometry can be used in both large-scale industry and biological applications (*in vitro* and *in vivo*).<sup>2-6</sup> Selecting a proper host matrix, as well as appropriate dopants, is important to achieve high performance and efficient energy transfer.<sup>7-9</sup> The photoluminescence emission of these Ln<sup>3+</sup>-doped NPs is expected to be quenched due to non-radiative relaxation via relaxation over the overtones of e.g. water or other solvents.<sup>10-12</sup> Doped core-inert shell particles are a common approach to enhance emission intensity and improve the performance of the Ln<sup>3+</sup>-doped NPs by protecting them from quenching, especially in water.<sup>1,4,6,12</sup> The inert shell shields the dopants against coupling with water overtones on the surface of the NPs.<sup>10-12</sup> Therefore, it is of utmost importance that no ion migration is present in the NPs, as this leads to emissive ions on the NP's surface and cancelling out the desired effect of the inert shell. In that case the expected core-shell particle would show the same behavior as a core only particle of the same size. A large variety of core-shell NP combinations have been reported up to date. The core material can be the same

as the shell material (homogenous) or different materials can be chosen for the core and the shell (heterogenous), however obtaining such heterogenous structures can be synthetically quite challenging.<sup>1-4</sup> Doped core-doped shell combinations are even more in need of precise doping, and therefore no ion migration can be present as their properties rely on the spatial separation of the dopants.<sup>13</sup>

The most researched upconversion (UC) material is  $\text{Er}^{3+}, \text{Yb}^{3+}:\text{NaYF}_4$  with the most commonly studied core-shell combination of  $\text{Er}^{3+}, \text{Yb}^{3+}:\text{NaYF}_4 @ \text{NaYF}_4$ . In  $\text{NaYF}_4$ , and also in  $\text{NaGdF}_4$ , ion migration has already been studied quite extensively.<sup>13,15-18</sup> Based on available literature we know that  $\text{NaYF}_4$  is mostly stable against ion migration with various dopants, however some reports claim otherwise. For example, de Sousa Ferreira *et al.* reported on complicated core-multi-shell  $\alpha\text{-NaY}_{0.85}\text{Dy}_{0.15}\text{F}_4 @ \alpha\text{-NaYF}_4 @ \beta\text{-NaGd}_{0.80}\text{Er}_{0.02}\text{Yb}_{0.18}\text{F}_4 @ \beta\text{-NaGd}_{0.75}\text{Nd}_{0.25}\text{F}_4$  NPs and investigated their integrity via scanning transmission electron microscopy (STEM) imaging with energy-dispersive X-ray (EDX) maps.<sup>13</sup> They found no significant migration of any of the afore mentioned ions in both  $\text{NaYF}_4$  and  $\text{NaGdF}_4$  host materials and further substantiated their findings by UC photoluminescence. Sun *et al.* reported on  $\text{NaYF}_4:\text{Yb}/\text{Tm} @ \text{NaErF}_4:\text{Ce} @ \text{NaYF}_4$  core-shell-shell nanoparticles for deep UV emission via the  $\text{NaErF}_4:\text{Ce}$  interlayer and an inert  $\text{NaYF}_4$  shell as protective layer.<sup>14</sup> The complicated structure was not investigated specifically in terms of ion migration, however, it also did not show any ion migration in the respective upconversion emission. Abel *et al.* reported on  $\text{NaYF}_4 @ \text{NaGdF}_4$  core-shell NPs via EDX line scans and electron energy loss spectroscopy (EELS), suggesting that neither  $\text{Y}^{3+}$  nor  $\text{Gd}^{3+}$  ions are migrating over the core-shell NPs.<sup>15</sup> Contrary to the findings presented above, Hudry *et al.* found significant ion migration in  $2\% \text{Er}, 20\% \text{Yb}:\text{NaGdF}_4 @ \text{NaYF}_4$  core-shell NPs.<sup>16</sup> Their STEM imaging combined with EDX maps, X-ray photoelectron spectroscopy (XPS) and X-ray total scattering suggests that

instead of sharp interfaces, interdiffusion of the inert shell through the core leads to an ion concentration gradient. In their work they also raise the question if different synthesis methods might influence this effect as the particle growth mechanism is different. Therefore, they questioned whether element intermixing is caused by the used synthesis method or if it is intrinsic. It was eventually suggested by the authors that it is likely a combination of both these factors. The element intermixing was later utilized by Hudry *et al.* for color tuning by variation of interface thickness of multi-shell  $\text{Er}^{3+}:\text{NaGdF}_4@\text{NaYbF}_4@\text{Tm}^{3+}:\text{NaGdF}_4@\text{NaYF}_4$  NPs.<sup>16</sup> They proved the different interface thicknesses via STEM and EDX line scans and luminescence lifetime measurements and saw similar results as in their earlier work. The element intermixing was observed for all ions and was significantly stronger for thicker shell materials, forming diffuse interface layers. The concentration gradient was also investigated via STEM and EDX maps and inductively coupled plasma mass spectrometry (ICP-MS) for  $\text{Yb}^{3+}$  in core only  $\text{Tm}^{3+}, \text{Yb}^{3+}:\text{NaYF}_4$  by Xu *et al.*<sup>18</sup> They found that  $\text{Yb}^{3+}$  is mostly concentrated in the core area building a radially decreasing concentration gradient to the outer shell of the particle. If a larger amount of  $\text{Yb}^{3+}$  was doped into the NPs the amount of  $\text{Yb}^{3+}$  migrating also increased, indicating a similar distribution gradient of  $\text{Yb}^{3+}$  for all doping percentages. This trend was also observed for different NP sizes. The influence of different synthesis methods was investigated by Hudry *et al.* for  $2\%\text{Er}^{3+}, 20\%\text{Yb}^{3+}:\text{NaYF}_4@\text{NaYF}_4(@\text{NaGdF}_4)$  core-(multi)-shell NPs.<sup>17</sup> They investigated hot injection thermal decomposition (method I), co-precipitation with acetates (method II) and shell precursors as sacrificial seeds (method III) and found that element intermixing is present for all the investigated synthesis methods. Pure core regions for core-shell  $2\%\text{Er}^{3+}, 20\%\text{Yb}^{3+}:\text{NaYF}_4@\text{NaYF}_4$  NPs made up for only 22%(I), 8%(II) and 36%(III) of the total volume whereas the amount of interface reached around 70% (method II). This finding was even

more elevated in multi-shell 2%Er<sup>3+</sup>,20%Yb<sup>3+</sup>:NaYF<sub>4</sub>@NaYF<sub>4</sub>@NaGdF<sub>4</sub> NPs, where for method II the pure core made up only 1% of the total volume, interface regions made up 34%, and the pure outer shell was 65% in total. These concentration gradients showed that rare earth (RE<sup>3+</sup>) ions that were supposed to be confined are in reality in direct contact with each other.

Li<sup>+</sup>-based host materials have in general been less studied than Na<sup>+</sup>-based materials, however, LiYF<sub>4</sub> and LiGdF<sub>4</sub> are matrices which have already been utilized for luminescence thermometry by other groups.<sup>19,20</sup> Shin *et al.* investigated the possibility of color tuning utilizing these host matrices while also confirming the core-multi-shell geometry via STEM and EDX maps.<sup>19</sup> Their STEM and EDX maps showed that ion migration in the Yb<sup>3+</sup>:LiYF<sub>4</sub>@Tm<sup>3+</sup>,Yb<sup>3+</sup>:LiGdF<sub>4</sub>@Eu<sup>3+</sup>:LiGdF<sub>4</sub>@LiYF<sub>4</sub> NPs was present for all elements. However, this phenomenon was not discussed and further investigated in detail within the publication. Nonetheless, color tuning was realized, indicating that a significant confinement was possible due to the interface regions from the Y<sup>3+</sup> to Gd<sup>3+</sup> containing host material. Some of us have recently reported on high temperature nanothermometers based on Er<sup>3+</sup>,Yb<sup>3+</sup>:LiLuF<sub>4</sub> and Er<sup>3+</sup>,Yb<sup>3+</sup>:LiLuF<sub>4</sub>@LiLuF<sub>4</sub> core-shell structures (with 3 or 6 shells).<sup>20</sup> To the best of our knowledge the occurrence of ion migration in LiLuF<sub>4</sub> had not been reported up until then. In our previous work we carried out STEM and EDX maps and temperature-dependent photoluminescence measurements, where we clearly observed that in the Er<sup>3+</sup>,Yb<sup>3+</sup>:LiLuF<sub>4</sub>@LiLuF<sub>4</sub> core-shell structures ion migration took place for both the Er<sup>3+</sup> and Yb<sup>3+</sup> ions. In our previous work, the ion migration had only been investigated for NPs prepared in a decomposition route when using trifluoroacetic acid precursors. It was suggested that the migration might be due to a self-purification process, a known phenomenon described in quantum dots where dopants migrate to the surface of the particles.<sup>21</sup>

Upon observing this problem in the  $\text{LiLuF}_4$  host in our previous study, we now focused on understanding the ion migration process and trying to find a solution to stop the doped emissive lanthanide ions from migrating in this host material. This was first tackled by changing the synthesis route and exploring the alternative co-precipitation synthesis approach, as well as a mixed co-precipitation-decomposition route for preparing the  $\text{Er}^{3+}, \text{Yb}^{3+}:\text{LiLuF}_4@\text{LiLuF}_4$  core-shell structures (core prepared using one route, shell prepared using the second route). Next, we considered building the inert shell from a different host material, in an attempt to stop the ion migration. This can however be a very challenging task from the synthetic point of view. It is best to choose a shell material which is still similar in the crystal structure to the core material.  $\text{LiYF}_4$  presents a similar crystal structure as  $\text{LiLuF}_4$  with both materials crystallizing in a scheelite structure.<sup>22,23</sup> The two host materials present good and also quite similar optical properties, with an expected lower up-conversion loss for the  $\text{LiLuF}_4$  NPs. It is important to mention that  $\text{LiLuF}_4$  shows a better resistance to optical damage compared to  $\text{LiYF}_4$ .<sup>22,24</sup>  $\text{LiGdF}_4$  is another shell material that is widely explored, but it can be very challenging to optimize in terms of morphology and homogeneous thickness as reported in previous studies.<sup>2-4</sup>

In this study the influence of the chosen synthesis route on the ion migration in  $2\% \text{Er}^{3+}, 18\% \text{Yb}^{3+}:\text{LiLuF}_4@\text{LiLuF}_4$  core-shell nanoparticles was investigated. Secondly, employing  $\text{LiYF}_4$  as the inert shell material to hinder or completely prevent ion migration was investigated.

To gain better understanding of the ion migration phenomenon in this particular host material, we investigated several doped core-inert shell and inert core-doped shell combinations:

$2\% \text{Er}^{3+}, 18\% \text{Yb}^{3+}:\text{LiLuF}_4@\text{LiLuF}_4,$   $\text{LiLuF}_4@2\% \text{Er}^{3+}, 18\% \text{Yb}^{3+}:\text{LiLuF}_4,$   
 $2\% \text{Er}^{3+}, 18\% \text{Yb}^{3+}:\text{LiLuF}_4@\text{LiYF}_4,$   $\text{LiLuF}_4@2\% \text{Er}^{3+}, 18\% \text{Yb}^{3+}:\text{LiYF}_4,$   
 $2\% \text{Er}^{3+}, 18\% \text{Yb}^{3+}:\text{LiYF}_4@\text{LiYF}_4,$   $\text{LiYbF}_4@\text{LiErF}_4$  and  $2\% \text{Er}^{3+}, 18\% \text{Yb}^{3+}:\text{NaYF}_4@\text{NaYF}_4.$  For

improved readability, in the following sections these combinations are named without the  $\text{Ln}^{3+}$  charges, and without the doping percentage, since those were held constant. The latter three materials were presented only for comparison reasons, as the reference material, or to validate our findings. An exciting application of UC NPs is their use as nanothermometers for various applications, ranging from biomedicine to nanoelectronics. Because of this important potential application, in the last part of our work we have also investigated the use of these core-shell materials as nanothermometers, aiming at high temperature thermometry.

## Results and Discussion

A schematic overview of the core and core-shell combinations developed in this work can be found in Fig. 1. The studied materials either undoped or doped  $\text{LiLuF}_4$  (light and dark purple, respectively) and undoped or doped  $\text{LiYF}_4$  (light and dark blue, respectively). The utilized doping percentage was 2%Er,18%Yb in both  $\text{LiLuF}_4$  and  $\text{LiYF}_4$  as this is a well-known UC ratio reported for many rare-earth fluoride materials.<sup>5,6</sup>

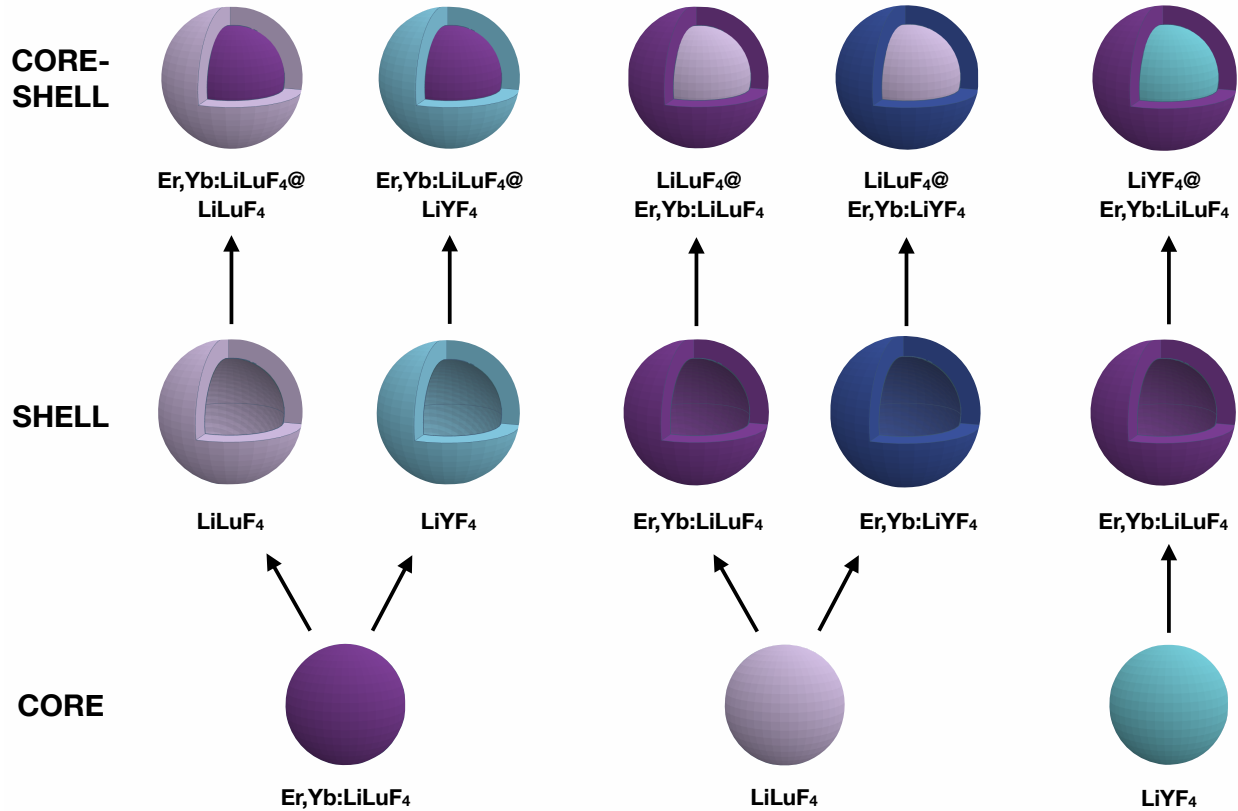


Fig. 1 Schematic illustration of the core (bottom row), shell (middle row) and core-shell combinations (top row) studied in this work.  $\text{Er,Yb:LiLuF}_4$  is shown in dark purple; undoped  $\text{LiLuF}_4$  is shown in light purple; undoped  $\text{LiYF}_4$  is shown in light blue;  $\text{Er,Yb:LiYF}_4$  is shown in dark blue.

$\text{LiLuF}_4$  crystallizes in a scheelite structure in the  $I41/a$  space group, isotopically to  $\text{LiYF}_4$ .<sup>22,23,26</sup> Eight  $\text{F}^-$  ions coordinate to the  $\text{Lu}^{3+}$  ion to form a slightly distorted square antiprism, as shown by Huang *et al.*<sup>27</sup> In this antiprism all the  $\text{Lu}^{3+}$  ions occupy a crystallographic 4b site with local  $S_4$  symmetry. A  $\text{LiLuF}_4$  single crystal has only been obtained at elevated pressure in its monoclinic fergusonite crystal structure.<sup>28</sup> Fig. 3 (a) shows the PXRD patterns of the  $\text{Er,Yb:LiLuF}_4@$  $\text{LiLuF}_4$  with cores prepared via the co-precipitation or thermal decomposition route in reference to the pattern generated from the 39563 ICSD data for  $\text{LiYF}_4$  as it crystallizes isotopically to scheelite

$\text{LiLuF}_4$ .<sup>22,23</sup> The PXRD patterns of the  $\text{Er,Yb:LiLuF}_4@\text{LiLuF}_4$  prepared via the co-precipitation route show that  $\text{LiLuF}_4$  NPs are formed.

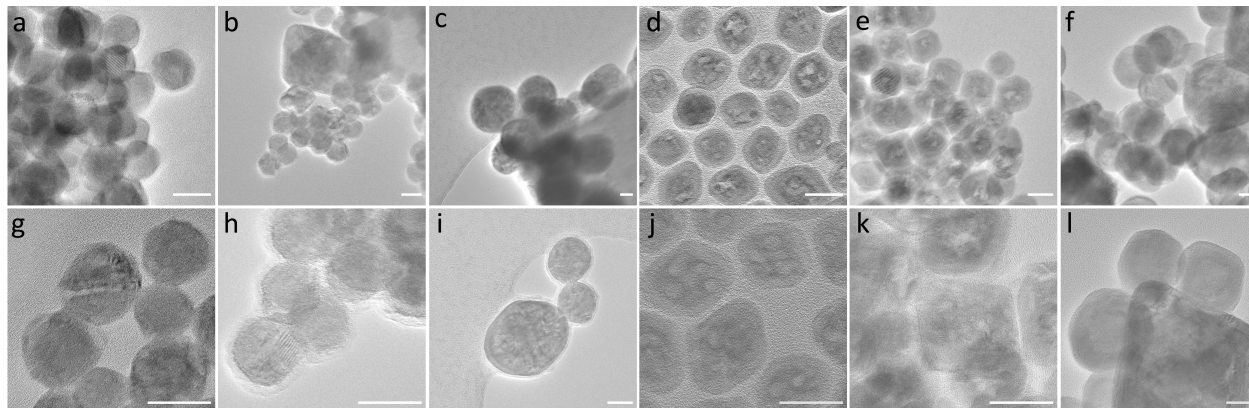


Fig. 2 Overview and magnified TEM images of (a), (g)  $\text{Er,Yb:LiLuF}_4@\text{LiLuF}_4$  where both the core and shell were obtained in the thermal decomposition route; (b), (h)  $\text{Er,Yb:LiLuF}_4@\text{LiLuF}_4$  where both the core and shell were obtained in the co-precipitation route; (c), (i)  $\text{LiLuF}_4@\text{Er,Yb:LiLuF}_4$  where both the core and shell were obtained in the co-precipitation route; (d), (j)  $\text{Er,Yb:LiLuF}_4@\text{LiYF}_4$  with the core from thermal decomposition route and the shell from co-precipitation route; (e), (k)  $\text{LiLuF}_4@\text{Er,Yb:LiYF}_4$  with both the core and shell from co-precipitation route; (f), (l)  $\text{LiYF}_4@\text{Er,Yb:LiLuF}_4$  with both core and shell from co-precipitation route. The corresponding high-resolution TEM images of the cores are shown in Fig. S3. The scale bar is 25 nm for all images.

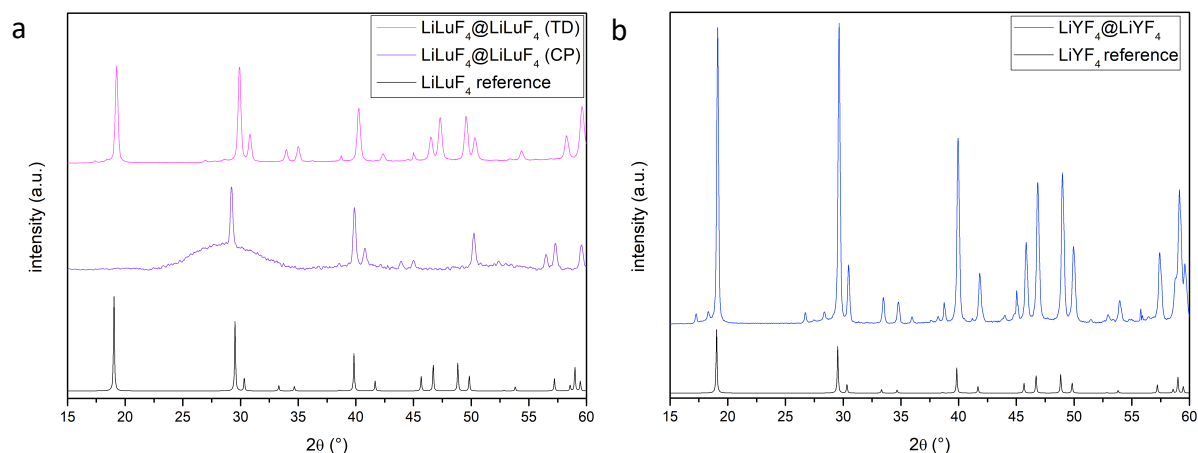


Fig. 3 PXRD patterns of the Er,Yb:LiLuF<sub>4</sub>@LiLuF<sub>4</sub> with shell and core prepared by thermal decomposition (indicated with “TD”) or co-precipitation (indicated with “CP”) (a) and Er,Yb:LiLuF<sub>4</sub>@LiYF<sub>4</sub> (b) compared with the 39563 ICSD reference data of LiYF<sub>4</sub><sup>22,23</sup>.

However, the PXRD additionally shows an amorphous band, indicating that the material is partly amorphous. The PXRD patterns of the Er,Yb:LiLuF<sub>4</sub>@LiLuF<sub>4</sub> NPs prepared via thermal decomposition route show no amorphous band, indicating better crystallinity. Both materials show diffraction peaks that correspond to the expected LiLuF<sub>4</sub> crystal structure.<sup>22,26</sup> The PXRD pattern of the Er,Yb:LiLuF<sub>4</sub>@LiYF<sub>4</sub> NPs prepared by thermal decomposition (core) and co-precipitation (shell) route is shown in Fig. 3 (b). The pattern matches the LiYF<sub>4</sub> reference data.<sup>22,23</sup> PXRD patterns for Er,Yb:LiYF<sub>4</sub>@LiYF<sub>4</sub>, LiErF<sub>4</sub>@LiYbF<sub>4</sub> and Er,Yb:NaYF<sub>4</sub>@NaYF<sub>4</sub> are shown in Fig. S1 and S2, respectively. They are also compared to the respective LiYF<sub>4</sub> or NaYF<sub>4</sub> reference. The PXRD patterns confirm that the expected materials were obtained. The peak position of all PXRD patterns show slight shifts compared to the reference data, which is to be expected, as those indicate lattice expansion (shift to the left) or contraction (shift to the right). The lattice expansions and contractions are expected upon doping of high percentages of Ln<sup>3+</sup> ions into the respective host lattices. LiLuF<sub>4</sub> incorporates the Er<sup>3+</sup> and Yb<sup>3+</sup> ions instead of Lu<sup>3+</sup> ions, which leads to a lattice

expansion (left shift) because the ions are larger compared to the host material.  $\text{LiYF}_4$  on the other hand experiences a lattice contraction (right shift) upon doping  $\text{Er}^{3+}$  and  $\text{Yb}^{3+}$  ions, because the  $\text{Y}^{3+}$  ion is smaller than the  $\text{Er}^{3+}$  and  $\text{Yb}^{3+}$  ions. The core-shell  $\text{LiLuF}_4@ \text{LiYF}_4$  PXRD patterns subsequently show no significant shift in peak positions.

TEM images of  $\text{LiLuF}_4@ \text{LiLuF}_4$  nanoparticles with different core-shell combinations prepared in two different synthesis routes (namely co-precipitation and thermal decomposition) are shown in Fig. 2. The schematic illustrations of the developed materials matching the description of the TEM images were shown in Fig. 1. The respective TEM images of the core corresponding to the core-shell nanoparticles is depicted in Fig. S3. The size of the corresponding core and core-shell nanoparticles can be found in Table 1, and the histograms showing the particle size distribution can be found in the SI (Fig. S7-S15). Since especially for the thermal decomposition synthesis route obtaining even nanoparticles is challenging, the nanoparticles presented are not homogenous in shape and size. However, as shown later in the work, these inhomogeneous samples were used in STEM and EDX mapping only as a proof of concept on suitable particles.

The  $\text{Er,Yb:LiLuF}_4@ \text{LiLuF}_4$  core-shell nanoparticles obtained in the thermal decomposition route are shown in Fig. 2(a). It is clear from the histograms (Fig. S7) that the size of the NPs increased significantly after the shelling procedure, indicating the formation of a core-shell nanomaterial with an average shell thickness around 8 nm. The  $\text{Er,Yb:LiLuF}_4@ \text{LiLuF}_4$  NPs obtained in the co-precipitation synthesis route are shown in Fig. 2(b).

Table 1: Average size of the short and long axis of the various materials prepared in the study, both as core (TEM images in Fig. S3) and core-shell combinations (TEM images in Fig. 2). The

respective histograms are presented in the SI (Fig. S7 to S15). The nanoparticles were prepared by thermal decomposition (indicated with “TD”) or co-precipitation (indicated with “CP”).

Materials	Core nanoparticles		Core-shell nanoparticles	
	short axis/diameter	long axis	short axis/diameter	long axis
Er,Yb:LiLuF <sub>4</sub> @LiLuF <sub>4</sub> core (CP)	23 nm	31 nm	26-30 nm	35 nm
Er,Yb:LiLuF <sub>4</sub> @LiLuF <sub>4</sub> core (TD)	15 nm	/	23 nm	/
LiLuF <sub>4</sub> @Er,Yb:LiLuF <sub>4</sub> core (CP)	46 nm	/	44 nm and 51 nm	/
Er,Yb:LiLuF <sub>4</sub> @LiYF <sub>4</sub>	21 nm	29 nm	27 nm	31 nm
LiLuF <sub>4</sub> @Er,Yb:LiYF <sub>4</sub>	21 nm	27 nm	42 nm	31 nm and 39 nm
LiYF <sub>4</sub> @Er,Yb:LiLuF <sub>4</sub>	15 nm	26 nm	35 nm	55 nm
LiErF <sub>4</sub> @LiYbF <sub>4</sub>	35 nm and 53 nm	62 nm and 72 nm	35, 68 and 72 nm	36 nm, 106 nm and 112 nm
Er,Yb:LiYF <sub>4</sub> @LiYF <sub>4</sub>	28 nm	48 nm	45 nm	53 nm
Er,Yb:NaYF <sub>4</sub> @NaYF <sub>4</sub>	31 nm	/	rod-like: 17 nm nm honey-comb: 23 nm	25- 40 nm

The histograms (Fig. S8) show that the size of the NPs increased significantly with the shelling procedure, indicating the formation of a core-shell structure with an average shell thickness around 5 nm. To investigate the ion migration process also a doped Er,Yb:LiLuF<sub>4</sub> shell around an undoped LiLuF<sub>4</sub> core was synthesized. The respective LiLuF<sub>4</sub>@Er,Yb:LiLuF<sub>4</sub> NPs are shown in Fig. 2(c). The average shell thickness is estimated to be around 5 nm (histogram in the SI, Fig. S9).

Core-shell NPs, where the host matrices LiYF<sub>4</sub> and LiLuF<sub>4</sub> were mixed (one used as core, and the other as shell), were grown to investigate the possible prevention of ion migration by the interface of a heterogeneous core-shell nanoparticle. Different crystal structures are expected to form a more efficient barrier for ion migration than a purely homogeneous core-shell structure would provide. The Er,Yb:LiLuF<sub>4</sub>@LiYF<sub>4</sub> NPs are shown in Fig. 2(d). The short axis grew around 6 nm on average, and the long axis grew around 2 nm on average (histogram in the SI, Fig. S10),

indicating that a shell was indeed successfully formed on the core nanoparticles. Fig. 2(e) shows the  $\text{LiLuF}_4@Er,Yb:LiYF_4$  material.

As reference materials  $Er,Yb:LiYF_4@LiYF_4$  and  $NaYF_4@NaYF_4$  NPs were also prepared. The homogeneous core-shell combination of  $NaYF_4@NaYF_4$  is researched here as well and has already been investigated regarding ion migration by other researcher groups.<sup>13,15-18</sup> This nanomaterial has been reported to show limited ion migration and can therefore be used as a reference material. Further, the homogeneous core-shell combination of  $LiYF_4@LiYF_4$  was chosen in order to compare the degree of ion migration in the presented  $Li^+$ -containing matrices  $LiLuF_4@LiLuF_4$ ,  $LiLuF_4@LiYF_4$  and  $LiYF_4@LiLuF_4$ . This is of importance because it is very challenging to grow shells of equal thickness and particles of the same size. Additionally, it was already shown by Hudry *et al.* that a thicker shell leads to a smaller pure core region.<sup>18</sup> Therefore, a good reference material is of great importance. The TEM images for these samples, and their respective histograms, can be found in the SI (TEM images: Fig. S4 and S5, histograms: Fig. S13 and S14). Both materials show successful shell formation with an average shell thickness of 17 nm (short axis) and 5 nm (long axis) ( $Er,Yb:LiYF_4@LiYF_4$ ) or up to 9 nm ( $Er,Yb:NaYF_4@NaYF_4$ ), respectively. A  $LiErF_4@LiYbF_4$  core-shell combination (images in the SI, TEM images: Fig. S6, histograms: Fig. S15) was also prepared to study ion migration in  $Li^+$ -containing matrices further. Here, also successful  $LiYbF_4$  shell formation is indicated around a  $LiErF_4$  core with an average thickness of up to 37 nm for the short axis and up to 50 nm for the long axis.

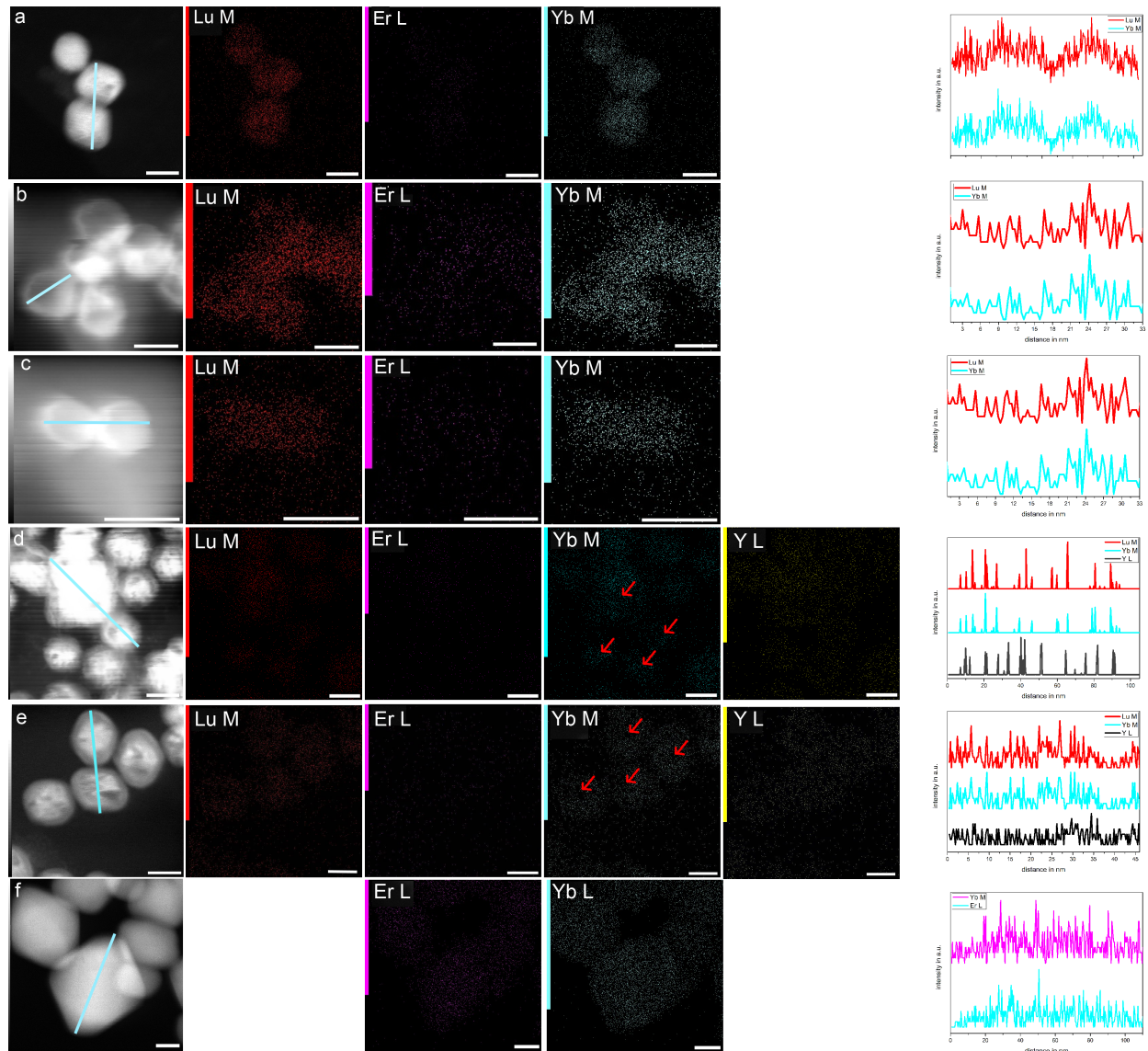


Fig. 4 STEM and EDX images and line scans of (a) Er,Yb:LiLuF<sub>4</sub>@ LiLuF<sub>4</sub> core from thermal decomposition route; (b), co-precipitation route; (c) LiLuF<sub>4</sub>@ Er,Yb:LiLuF<sub>4</sub>. (d) Shows the Er,Yb:LiLuF<sub>4</sub>@LiYF<sub>4</sub>; (e) shows the LiLuF<sub>4</sub>@ Er,Yb:LiYF<sub>4</sub>; (f) shows the LiErF<sub>4</sub>@LiYbF<sub>4</sub> core-shell structure. The respective line scans are shown in the right column. The scalebar is 25 nm for all images. Only the LiLuF<sub>4</sub>@LiYF<sub>4</sub> core-shell combination shows sufficiently suppressed ion migration; areas of interest are marked with red arrows.

In Fig. 4 various STEM and EDX maps, and the respective line scans, for the  $\text{LiLuF}_4@ \text{LiLuF}_4$  and  $\text{LiLuF}_4@ \text{LiYF}_4$  core-shell combinations are shown. Fig. 4 (a) depicts the  $\text{Er,Yb:LiLuF}_4@ \text{LiLuF}_4$  with the core from thermal decomposition and the shell from co-precipitation synthesis. Fig. 4(b) shows the same combination, but with a core prepared using the co-precipitation route. The  $\text{LiLuF}_4@ \text{Er,Yb:LiLuF}_4$  prepared in co-precipitation synthesis is shown in Fig. 4 (c). For all these NPs the core and the shell are not distinguishable in terms of  $\text{Er}^{3+}$  and  $\text{Yb}^{3+}$  ions (indicated in purple and yellow, respectively), indicating ion migration over the whole nanoparticles. Therefore, unfortunately, a different synthesis route compared to that investigated in our last study, seems to be unable to hinder ion migration in  $\text{LiLuF}_4$ . It can therefore be concluded that ion migration is not synthesis route dependent for the homogeneous  $\text{Er,Yb:LiLuF}_4@ \text{LiLuF}_4$  nanoparticles. Fig. 4 (d) shows the STEM and EDX maps for the  $\text{Er,Yb:LiLuF}_4@ \text{LiYF}_4$  NPs. The overlapped signals for Lu, Yb and Y are shown in Fig. S17 in the SI for more clarity. Fig. 4 (e) shows the reversely doped  $\text{LiLuF}_4@ \text{Er,Yb:LiYF}_4$  geometry. The overlapped signals for Er, Yb and Y are shown in Fig. S18 in the SI for clarity. Both  $\text{LiLuF}_4@ \text{LiYF}_4$  doped core-undoped shell and undoped core-doped shell combinations show significantly less ion migration compared to the doped core-undoped shell and undoped core-doped shell  $\text{LiLuF}_4@ \text{LiLuF}_4$  combinations, which is likely caused by the interface region of the former. However,  $\text{Yb}^{3+}$  ions are still present in areas that were expected to be inert, marked with red arrows in Fig. 4. This strongly suggests that some ion migration is still present and cannot be completely prevented even by an interface. The STEM and EDX maps for Lu (Fig. 4 (d) and (e) in red) and Y (Fig. 4 (d) and (e) in yellow) also show that these ions are present in areas that should only show Y or Lu respectively.  $\text{Lu}^{3+}$  and  $\text{Y}^{3+}$  ions are found also in the inner parts of the particles, indicating

that not only  $\text{Yb}^{3+}$  and  $\text{Er}^{3+}$ , but also  $\text{Lu}^{3+}$  and  $\text{Y}^{3+}$  migrate over the NPs. The migration, however, is less severe.

These important findings might indicate that  $\text{LiLuF}_4$  and  $\text{LiYF}_4$  as matrix materials themselves are not stable against ion migration and do not sufficiently hold dopants in the crystal structure when designing core-shell structures. To further investigate this claim, the prepared reference materials ( $\text{Er,Yb:LiYF}_4@\text{LiYF}_4$ ,  $\text{Er,Yb:NaYF}_4@\text{NaYF}_4$  and  $\text{LiErF}_4@\text{LiYbF}_4$ ) were also studied for ion migration. First, the  $\text{Er,Yb:LiYF}_4@\text{LiYF}_4$  was evaluated with STEM and EDX. Fig. 4 (f) strongly indicates that this core-shell combination shows ion migration, as already suggested but not further discussed in literature<sup>19</sup>. In order to further investigate host materials containing  $\text{Li}^+$ , the  $\text{LiErF}_4@\text{LiYbF}_4$  core-shell material was synthesized and investigated via STEM and EDX maps Fig. 4 (g). These EDX maps show significant ion migration for both  $\text{Yb}^{3+}$  and  $\text{Er}^{3+}$ , suggesting that indeed  $\text{Li}^+$  enables ion migration in fluoride host materials. As an additional reference, and to investigate the claim of lithium adding to the instability of the host material, the well-studied  $\text{Er,Yb:NaYF}_4@\text{NaYF}_4$  was also investigated using STEM and EDX maps (Fig. S16). This combination does not show any noticeable ion migration, which is in good agreement with observations already reported in literature.<sup>13-18</sup>  $\text{Na}^+$ -containing matrices (e.g.  $\text{NaYF}_4$  and  $\text{NaGdF}_4$ ) have proven to form interface regions but also to retain some limited inert core/shell regions. In comparison,  $\text{Li}^+$ -containing matrices such as  $\text{LiLuF}_4$ <sup>20</sup> and  $\text{LiYF}_4$ <sup>18</sup> seem to suffer greatly from ion migration.<sup>13-18</sup> A doped core-undoped shell and undoped core-doped shell with  $\text{LiLuF}_4@\text{LiYF}_4$  or  $\text{LiYF}_4@\text{LiLuF}_4$  combination seems to suppress ion migration greatly, but even these heterogenous core-shell structures are not able to prevent it completely as we have shown in our study. However, it is a good solution for decreasing the ion migration in these host materials and allowing the development of true core-shell structures. At this point it must be pointed out that also the widely

used Na<sup>+</sup>-containing matrices like NaYF<sub>4</sub> can suffer from ion migration to an extent (e.g. when very small core-shell nanoparticles are developed), however this is not always mentioned or elaborated on in literature.<sup>13-18</sup> The ion migration in those materials is however not very significant, and therefore unable to influence the photoluminescence to such an extent as the here presented Li<sup>+</sup>-containing matrices. Additionally, only when carrying out comparative studies, or high temperature luminescence studies, some of these phenomena will be clearly visible. Nevertheless, as a good rule, the lack of ion migration should always be ruled out based on meticulous analysis of every core-shell nanomaterial, and best this should be done for every batch of materials, as varying size of the core and shell can have an impact here.

To further confirm our observations made based on STEM and EDX results, which show the growth of a LiYF<sub>4</sub> inert shell significantly hinders the ion migration process, the emission spectra of selected doped core-undoped shell combinations (Fig. 5(a) Er,Yb:NaYF<sub>4</sub>@NaYF<sub>4</sub>, (b) Er,Yb:LiLuF<sub>4</sub>@LiLuF<sub>4</sub>, (c) Er,Yb:LiLuF<sub>4</sub>@LiYF<sub>4</sub> and (d) Er,Yb:LiYF<sub>4</sub>@LiYF<sub>4</sub>) were measured in the temperature range from 280 K to 480 K (step size of 20 K). The measurements were carried out to further substantiate the findings on ion migration presented in Fig. 4 and Fig. S16 to S18. For a doped core-inert shell material without ion migration it is expected that with increasing temperature the intensity of luminescence is progressively quenched through the thermal quenching process.<sup>20,29</sup>

This is especially the case for nano-sized particles as the surface-to-volume ratio is much higher compared to micro-sized or bulk materials. However, if the emissive ions migrate from the protected core to the surface of the nanoparticle, their luminescence is expected to additionally be quenched by water molecules that are adsorbed on the surface of the NPs. This so-called environmental quenching is caused by relaxation via OH-vibrations, causing a coupling of

luminescence centers and their environment. With increasing temperature, the water molecules will slowly start to evaporate from the surface of the NPs and the emissive ions on the surface of the NPs will no longer be environmentally quenched, but only be affected by thermal quenching. This gives rise to different behavior in the emission maps recorded over a range of temperatures and allows us to verify in which materials we most likely observe ions migrating to the inert shell. The onset of water molecule evaporation is expected to be around 340 K. Therefore, ion migration of emissive ions to the surface of the nanoparticles would be further indicated by a thermal enhancement of the photoluminescence around 340 K to 360 K as it is described in the overview by Shi *et al.*<sup>29</sup> and as observed and reported by Kaczmarek *et al.*<sup>20</sup> The later showed that this behavior is only present in air but not in nitrogen atmosphere, linking it closely to the medium surrounding the nanoparticle.

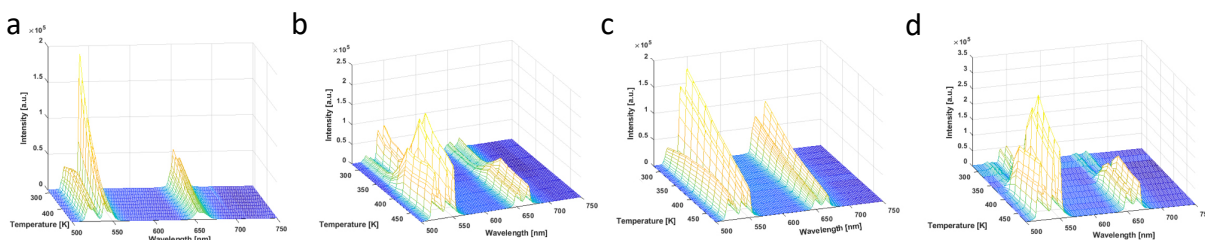


Fig. 5 Emission maps of the  $\text{Er,Yb:NaYF}_4@\text{NaYF}_4$  (a),  $\text{Er,Yb:LiLuF}_4@\text{LiLuF}_4$  (b),  $\text{Er,Yb:LiLuF}_4@\text{LiYF}_4$  (c) and  $\text{Er,Yb:LiYF}_4@\text{LiYF}_4$  (d) recorded from 280 K to 480 K with a step size of 20 K in solid after ligand removal.

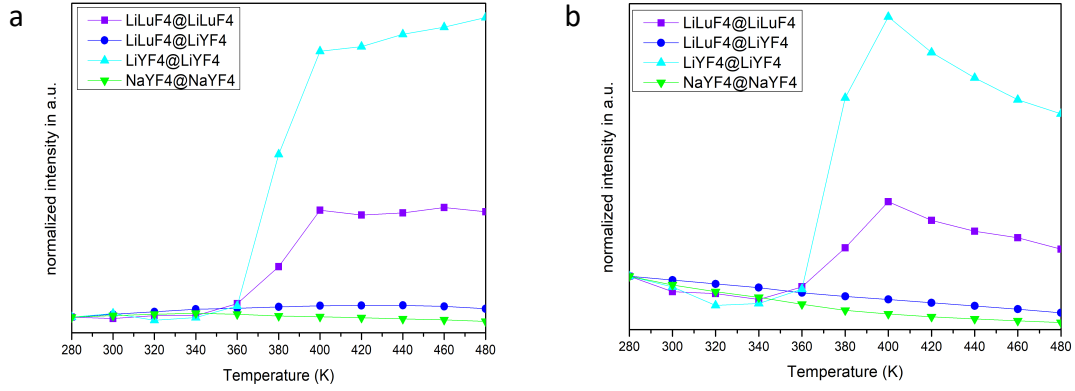


Fig. 6 Intensity of the  ${}^2\text{H}_{11/2} \rightarrow {}^4\text{I}_{15/2}$  (520 nm) transition (a) and for the  ${}^4\text{S}_{3/2} \rightarrow {}^4\text{I}_{15/2}$  (550 nm) transition (b) for Er,Yb:LiLuF<sub>4</sub>@LiLuF<sub>4</sub>, Er,Yb:LiLuF<sub>4</sub>@LiYF<sub>4</sub>, Er,Yb:LiYF<sub>4</sub>@LiYF<sub>4</sub> and Er,Yb:NaYF<sub>4</sub>@NaYF<sub>4</sub>. The intensities are normalized to the 280 K intensity of each sample respectively. The raw data is shown in Fig. S19. The lines are a guideline for the eye. The highest intensity is reached around 380-400 K, where water evaporation from the surface of the sample is completed.

In Fig. 5 the emission maps of Er,Yb:NaYF<sub>4</sub>@NaYF<sub>4</sub> (a) Er,Yb:LiLuF<sub>4</sub>@LiLuF<sub>4</sub> (b), Er,Yb:LiLuF<sub>4</sub>@LiYF<sub>4</sub> (c) and Er,Yb:LiYF<sub>4</sub>@LiYF<sub>4</sub> (d) are shown. We have additionally calculated the respective thermometric parameters  $\Delta$  and  $S_r$  for these materials (Fig. S19), as thermometry is an important application of many lanthanide-doped NPs. The respective intensities, normalized to their 280 K intensity, are shown in Fig. 6 for the  ${}^2\text{H}_{11/2} \rightarrow {}^4\text{I}_{15/2}$  transition at 520 nm and for the  ${}^4\text{S}_{3/2} \rightarrow {}^4\text{I}_{15/2}$  transition at 550 nm, the raw data has been plotted in Fig. S19. A respective temperature map for LiErF<sub>4</sub>@LiYbF<sub>4</sub> was recorded and is shown in Fig. S20. However, it showed an insufficient goodness of fit, indicating poor thermometry properties. This is most likely due to the incorrect ratio of the Er<sup>3+</sup> and Yb<sup>3+</sup> dopants suited for successful UC luminescence. The ideal doping percentage is 2%Er and 18%Yb, giving a ratio of 1 Er<sup>3+</sup>:9 Yb<sup>3+</sup>. In the presented core-shell

particles, the core-to-shell ratio and respective Yb:Er ratio is significantly higher. A good thermometric performance was therefore not expected, but this sample was prepared mostly as a reference material for use for EDX maps. Additionally, the dopants were spread throughout the whole NP and the intensity was low due to pronounced concentration quenching. The emission map of Er,Yb:NaYF<sub>4</sub>@NaYF<sub>4</sub> (a) shows a linear drop in luminescence intensity from 280 K to 480 K for all peaks. Fig. 6 shows that the intensity, normalized to 280 K, does not vary greatly with increasing temperature. This behavior was expected and indicates that the NaYF<sub>4</sub> core-shell NPs show no or no significant ion migration from the core to the surface of the core-shell particles, where the luminescence of the emissive ions could get quenched by water molecules at room temperature. The emission map of Er,Yb:LiLuF<sub>4</sub>@LiLuF<sub>4</sub> (Fig. 5(b)) shows a slight drop in luminescence intensity from 280 K to 320 K followed by a sharp increase in intensity around the expected temperature of water evaporation at an onset of 340 K until 450 K where it reaches a saturation that is continued to 480 K. This behavior indicates that indeed emissive ions migrate from the core to the outer surface (the shell) of the core-shell particles, where their luminescence is quenched by water molecules at room temperature. At elevated temperatures the water starts to evaporate, leading to thermal enhancement due to weaker intensity quenching of the emissive ions. The enhancement of the intensity is also shown in Fig. 6 where both transitions show a great enhancement above 360 K. This strongly suggests that ion migration is present in LiLuF<sub>4</sub>@LiLuF<sub>4</sub> and confirms the STEM and EDX findings.

The emission map of Er,Yb:LiLuF<sub>4</sub>@LiYF<sub>4</sub> (c) shows a linear drop in luminescence intensity from 280 K to 480 K for all peaks. This behavior was expected since significantly less ion migration was stated from the STEM and EDX maps in Fig. 4 for this core-shell combination. It is therefore assumed that LiYF<sub>4</sub> is able to significantly hinder ion migration as an inert shell

material for  $\text{LiLuF}_4$ . Fig. 6 also shows a similar trend for  $\text{Er,Yb:LiLuF}_4@\text{LiYF}_4$  as observed in the  $\text{Er,Yb:NaYF}_4@\text{NaYF}_4$  reference material for both green transitions peaks, but with no increase in intensity with temperature increase. However, the drop in intensity is slightly less pronounced for both electronic transitions compared to  $\text{Er,Yb:NaYF}_4@\text{NaYF}_4$ . This suggests that in the heterogeneous  $\text{Er,Yb:LiLuF}_4@\text{LiYF}_4$  NPs the ion migration is yet still more pronounced than in the homogeneous  $\text{Er,Yb:NaYF}_4@\text{NaYF}_4$ . This was already suggested by the STEM and EDX maps, as discussed before.

The emission map for  $\text{Er,Yb:LiYF}_4@\text{LiYF}_4$  (Fig. 4 (d)) shows a similar trend to that of the  $\text{Er,Yb:LiLuF}_4@\text{LiLuF}_4$ . The change in luminescence intensity with temperature increase depicted in Fig. 6 shows a similar behavior as described previously for  $\text{Er,Yb:LiLuF}_4@\text{LiLuF}_4$ : The luminescence intensity first slightly drops with increasing temperature until a rapid increase in intensity is observed above 360 K. The trend is even more pronounced for  $\text{Er,Yb:LiYF}_4@\text{LiYF}_4$ . This validates the findings presented by the EDX maps in Fig. 4 and suggests that strong ion migration takes place not only in  $\text{LiLuF}_4@\text{LiLuF}_4$ , but also in  $\text{LiYF}_4@\text{LiYF}_4$  NPs. This later material has been studied quite extensively in literature, but the ion migration phenomenon has not been reported up till now.

To confirm that the above described behavior is not due to thermal degradation but rather indicates ion migration, the PXRD patterns for  $\text{Er,Yb:LiLuF}_4@\text{LiLuF}_4$  and  $\text{Er,Yb:LiLuF}_4@\text{LiYF}_4$  after the heating-cooling cycle tests were carried out are shown in Fig. S22 to confirm the stability of the crystal structure. No significant change in crystal structure can be observed. Therefore, the presence of thermal degradation and consequent ion migration due to elevated temperatures cannot be substantiated. It has also been shown previously by Kaczmarek *et al.*, that  $\text{LiLuF}_4$  exhibits stable

performance not only in air but also nitrogen when cycling in the here presented temperature regime of 280 to 480 K.<sup>20</sup>

In order to substantiate these findings, decay time measurements for Er,Yb:LiLuF<sub>4</sub>@LiLuF<sub>4</sub> and Er,Yb:LiYF<sub>4</sub>@LiYF<sub>4</sub>, Er,Yb:LiLuF<sub>4</sub>@LiYF<sub>4</sub> and LiLuF<sub>4</sub>@Er,Yb:LiYF<sub>4</sub> were performed and compared to their Er,Yb:LiLuF<sub>4</sub> and Er,Yb:LiYF<sub>4</sub> core only nanoparticles. The data for all relevant electronic transitions is shown in Fig. S23 in the SI. The respective decay time values and goodness of fit R<sup>2</sup> are shown in Table S1. An inert LiLuF<sub>4</sub> or LiYF<sub>4</sub> shell was expected to increase the lifetimes significantly when compared to the core only nanoparticles since then the doped core is significantly more protected from the environment. Therefore, it was assumed that the heterogeneous core-shell material would offer longer lifetimes when compared to the homogeneous core-shell combinations, and also compared to their respective core-only materials. Additionally, in general, an increased in size of the respective nanoparticle is linked to an increase in lifetime.<sup>3</sup> Subsequently, a drop in luminescence lifetime would suggest that the emissive Ln<sup>3+</sup> ions are less protected from the environment. Additionally, it is known that the breaking of local symmetry and a lower extend of crystallinity also lowers the respective lifetime, as suggested by Dong *et al.*<sup>31</sup>

The lifetimes of the Er,Yb:LiLuF<sub>4</sub> and Er,Yb:LiYF<sub>4</sub> core nanoparticles were calculated to be 188  $\mu$ s, 239  $\mu$ s, 952  $\mu$ s (Er,Yb:LiLuF<sub>4</sub>) and 448  $\mu$ s and 473  $\mu$ s, 723  $\mu$ s (Er,Yb:LiYF<sub>4</sub>), respectively, for the different Er<sup>3+</sup> transition peaks (see Table S1). These lifetimes are in good agreement with values from literature for the respective host materials.<sup>21,30</sup> The homogeneous Er,Yb:LiLuF<sub>4</sub>@LiLuF<sub>4</sub> (389  $\mu$ s, 390  $\mu$ s, 498  $\mu$ s). and Er,Yb:LiYF<sub>4</sub>@LiYF<sub>4</sub> (619  $\mu$ s, 626  $\mu$ s, 705  $\mu$ s) show a significant increase in lifetime compared to their respective doped core only nanoparticles. This is most likely caused, as previously pointed out, only by an increase in size and

not by a more protected emissive core. This claim is substantiated by comparing the lifetimes of the homogeneous core-shell particles to the heterogeneous Er,Yb:LiLuF<sub>4</sub>@LiYF<sub>4</sub> core-shell nanoparticle. The heterogeneous combination shows the highest lifetimes of all the investigated nanoparticles, indicating highly protected emissive Ln<sup>3+</sup> ions in the core. This suggests that there is only very little ion migration in this heterogeneous core-shell type of nanoparticle.

The heterogeneous LiLuF<sub>4</sub>@Er,Yb:LiYF<sub>4</sub> combination was also investigated (343  $\mu$ s, 345  $\mu$ s, 413  $\mu$ s) to exclude the possibility of an increase in lifetime mainly caused by an increase in the size of the nanoparticles. For this the heterogeneous combination was compared to its Er,Yb:LiLuF<sub>4</sub>@LiYF<sub>4</sub> counterpart and respective doped Er,Yb:LiYF<sub>4</sub> core. The inert core-doped shell combination performs significantly worse with lifetimes comparable to the homogeneous Er,Yb:LiLuF<sub>4</sub>@LiLuF<sub>4</sub>, which shows excessive ion migration. The lifetimes are lower than the ones for the respective core most likely due to a break of local symmetry at the interface region, and a smaller size of the emissive area. This comparison substantiates the claim that the respective emissive Ln<sup>3+</sup> ions are less protected from the environment in both the homogeneous Er,Yb:LiLuF<sub>4</sub>@LiLuF<sub>4</sub> and the emissive shell of the LiLuF<sub>4</sub>@Er,Yb:LiYF<sub>4</sub>. Therefore, we can state that the heterogeneous Er,Yb:LiLuF<sub>4</sub>@LiYF<sub>4</sub> combination performs superior compared to not only the homogeneous core-shell combinations but also compared to its respective Er,Yb:LiLuF<sub>4</sub> and Er,Yb:LiYF<sub>4</sub> core-only nanoparticles. The longer lifetimes confirm significantly reduced ion migration in the heterogeneous core-shell combination and increased protection by a shell made from a different material.

Additionally, XRF measurements of Er,Yb:LiLuF<sub>4</sub>@LiLuF<sub>4</sub>, Er,Yb:LiYF<sub>4</sub>@LiYF<sub>4</sub> and Er,Yb:LiLuF<sub>4</sub>@LiYF<sub>4</sub> were performed and compared to their respective Er,Yb:LiLuF<sub>4</sub> and Er,Yb:LiYF<sub>4</sub> cores. Their respective spectra and calculated element percentages are shown in Fig.

S24 and Table S2. The data shows that the core nanoparticles are stoichiometrically doped (1.9% and 2.4%  $\text{Er}^{3+}$  with 2%  $\text{Er}^{3+}$  expected; and 19.8% and 21%  $\text{Yb}^{3+}$  with 20%  $\text{Yb}^{3+}$  expected). For  $\text{Er,Yb:LiLuF}_4@\text{LiLuF}_4$  0.6%  $\text{Er}^{3+}$ , 6.7%  $\text{Yb}^{3+}$  and 92.5%  $\text{Lu}^{3+}$  was measured when stoichiometrically expected values were: 1.3%  $\text{Er}^{3+}$ , 12%  $\text{Yb}^{3+}$  and 86.7%  $\text{Lu}^{3+}$ . For  $\text{Er,Yb:LiYF}_4@\text{LiYF}_4$  1.6%  $\text{Er}^{3+}$ , 13.1%  $\text{Yb}^{3+}$  and 85.3%  $\text{Y}^{3+}$  was measured when stoichiometrically expected values were: 1.3%  $\text{Er}^{3+}$ , 12%  $\text{Yb}^{3+}$  and 86.7%  $\text{Y}^{3+}$ . And for the heterogeneous  $\text{Er,Yb:LiYF}_4@\text{LiYF}_4$  nanoparticles 0.36%  $\text{Er}^{3+}$ , 13.1%  $\text{Yb}^{3+}$ , 59.5%  $\text{Lu}^{3+}$  and 27.0%  $\text{Y}^{3+}$  were measured when stoichiometrically expected values were: 1.3%  $\text{Er}^{3+}$ , 12%  $\text{Yb}^{3+}$ , 53.3%  $\text{Lu}^{3+}$  and 33.3%  $\text{Y}^{3+}$ . Therefore, the  $\text{Er,Yb:LiLuF}_4@\text{LiLuF}_4$  shows a shortage of  $\text{Er}^{3+}$  and  $\text{Yb}^{3+}$ , suggesting that the core  $\text{RE}^{3+}$  are at least partially lost while shelling. This suggests a “cation exchange mechanism”, as presented by Dong *et.al.*<sup>32</sup> This mechanism was described for  $\text{LaF}_3$  nanoparticles that were exposed to  $\text{Ln}^{3+}$  in aqueous media. During synthesis, the  $\text{La}^{3+}$  ions of the host material were replaced quickly with the solvated  $\text{RE}^{3+}$  ions, while the  $\text{La}^{3+}$  ions (now solvated in the aqueous solvent) were not able to incorporate back fast enough to reach equilibrium. This led to a shortage of  $\text{La}^{3+}$  ions (which formed the core material) in the synthesized nanoparticles. It was therefore expected that XRF would show a significantly lower doping percentage of  $\text{Er}^{3+}$  and  $\text{Yb}^{3+}$  as stoichiometrically weighted off for the homogenous core-shell combinations, while the doping percentage of  $\text{Lu}^{3+}/\text{Y}^{3+}$  of the shell ions was expected to be higher than stoichiometrically weighted off. In other words, it was expected that the  $\text{RE}^{3+}$  ions of the host material ( $\text{Er}^{3+}$ ,  $\text{Yb}^{3+}$  and  $\text{Lu}^{3+}/\text{Y}^{3+}$ ) were replaced with the  $\text{RE}^{3+}$  ions of the shell ( $\text{Lu}^{3+}/\text{Y}^{3+}$ ). However, the homogeneous  $\text{Er,Yb:LiYF}_4@\text{LiYF}_4$  shows the expected doping percentages, indicating that no ion exchange mechanism is present. This can be explained by the different synthesis route of the core from coprecipitation as compared to the core from thermal decomposition. We were not able to

differentiate those two synthesis methods via the STEM EDX images, but it is likely that the mechanism of shelling is different for the two routes, leading to a different mechanism of ion migration in the nanoparticles. The exact mechanism of ion migration in these Li<sup>+</sup>-based host materials will still need further investigation to draw final conclusions. It is however most likely that a cation exchange process takes place during synthesis, as previously described in literature.<sup>32</sup> Additionally, the migration is expected to depend on the crystallization and its temperature as well as possible defects in the matrix and the shell thickness. Hudry *et al.* studied the influence of those factors on Na<sup>+</sup>-containing nanoparticles.<sup>16,17</sup> It is expected that Li<sup>+</sup>-containing matrices show a similar behavior. The heterogeneous Er,Yb:LiLuF<sub>4</sub>@LiYF<sub>4</sub> shows doping percentages of all elements within the expected range, indicating no significant ion exchange. Consequently, only very little ion migration occurs during the synthesis. This further substantiates our claim of excessive ion migration in the homogenous Er,Yb:LiLuF<sub>4</sub>@LiLuF<sub>4</sub> core-shell nanoparticles and limited ion migration in the Er,Yb:LiLuF<sub>4</sub>@LiYF<sub>4</sub> core-shell nanoparticles.

Therefore, it is suggested that Li<sup>+</sup> as ion in the matrix might be the cause of the elevated ion migration in both LiLuF<sub>4</sub> and LiYF<sub>4</sub>. It has been reported, and also observed by us in this study, that NaYF<sub>4</sub> is able to form true doped core-undoped shell geometries, although a small amount of ion migration in these materials can also be observed. It was already suggested by Shi *et al.* that the difference in ionic radii of the Ln<sup>3+</sup> is the most important factor to hinder ion migration in matrices.<sup>29</sup> Our experiments suggest however that this is not the only factor, as the ions also migrate in LiYF<sub>4</sub>, with Y<sup>3+</sup> having a different ionic radii compared to Lu<sup>3+</sup>. Moreover, the matrices containing Li<sup>+</sup> seem to in general be more prone to ion migration. This instability might be due to the fact that in LiLuF<sub>4</sub> and LiYF<sub>4</sub> the Li<sup>+</sup> is coordinated 4-times, whereas in the NaYF<sub>4</sub> matrix the Na<sup>+</sup> is coordinated 8-fold, leading to a more stable position of Na<sup>+</sup> ions in the matrix. Additionally,

the difference in ionic radii is smaller for  $\text{Li}^+$  (28% for  $\text{Y}^{3+}$ , 17.98% for  $\text{Er}^{3+}$ , 15.9% for  $\text{Yb}^{3+}$ , 15.2% for  $\text{Lu}^{3+}$ ) than for  $\text{Na}^+$  (23% for  $\text{Y}^{3+}$ , 32.6% for  $\text{Er}^{3+}$  and 34.2% for  $\text{Yb}^{3+}$ ), leading to easier ion migration in  $\text{Li}^+$ -containing matrices as they provide vacancies that are more easily occupied.<sup>22,23,28</sup> However, an interface between both materials ( $\text{LiLuF}_4$  and  $\text{LiYF}_4$ ) seems to be able to hinder the migration sufficiently to improve the photoluminescence properties of the respective core-shell nanoparticles.

The influence of ion migration on the photoluminescence suggests that  $\text{LiYF}_4$  might be even more prone to ion migration than  $\text{LiLuF}_4$ , however the differences might not be due to inherent material differences.  $\text{LiYF}_4$  was expected to hinder ion migration more sufficiently than  $\text{LiLuF}_4$  because of a larger difference in the ionic radii for  $\text{Yb}^{3+}$  (14.14% with  $\text{Y}^{3+}$  and 1% with  $\text{Lu}^{3+}$ ) and  $\text{Er}^{3+}$  (12% with  $\text{Y}^{3+}$  and 3.3% with  $\text{Lu}^{3+}$ ). However, these difference in ionic radii only differ around 2%, and therefore the difference in ion migration severity might not be sufficiently noticeable. Despite these considerations the reverse is shown in the emission maps with a great difference for  $\text{Er,Yb:LiLuF}_4@\text{LiLuF}_4$  and  $\text{Er,Yb:LiYF}_4@\text{LiYF}_4$ . As indicated by the comparison of the heterogeneous  $\text{Er,Yb:LiYF}_4@\text{LiLuF}_4$  with the  $\text{Er,Yb:NaYF}_4@\text{NaYF}_4$ , these findings might hold actual information of the severity of ion migration in the samples, as the two materials differ slightly in their behavior regarding their normalized intensity.

## Conclusions

In this work we aimed at studying in detail the ion migration phenomenon in the  $\text{LiLuF}_4$  host matrix. This was done for 2%Er,18%Yb-doped  $\text{LiLuF}_4$  nanoparticles, and compared with several other host materials and core-shell combinations. First, we investigated whether ion migration in this host could be hindered by selecting different synthesis routes. STEM and EDX findings

suggested that a variation in synthesis route alone for the preparation of either core and/or shell does not hinder ion migration significantly in the core-shell structures. We further prepared and characterized various Li<sup>+</sup>-containing materials in different core-shell combinations. Er,Yb:LiLuF<sub>4</sub>@LiLuF<sub>4</sub> and LiLuF<sub>4</sub>@Er,Yb:LiLuF<sub>4</sub>, Er,Yb:LiYF<sub>4</sub>@LiYF<sub>4</sub>, and LiErF<sub>4</sub>@LiYbF<sub>4</sub> showed pronounced ion migration, suggested by STEM and EDX maps as well as high temperature photoluminescence measurements and decay times measurements. The heterogeneous core-shell combinations Er,Yb:LiLuF<sub>4</sub>@LiYF<sub>4</sub>, Er,Yb:LiYF<sub>4</sub>@LiLuF<sub>4</sub>, LiLuF<sub>4</sub>@Er,Yb:LiYF<sub>4</sub> and LiYF<sub>4</sub>@Er,Yb:LiLuF<sub>4</sub> showed only a small amount of ion migration. These results were compared with the well-researched Er,Yb:NaYF<sub>4</sub>@NaYF<sub>4</sub>, which is expected to show no or only very little ion migration. These claims were further substantiated by lifetime and XRF measurements and careful analysis. These findings suggest that Li<sup>+</sup>-containing matrices are more prone to ion migration than Na<sup>+</sup>-containing matrices. This difference might be explained by a greater difference in ionic radii of Na<sup>+</sup> ions to the RE<sup>3+</sup> ionic radii, as well as the higher coordination number of Na<sup>+</sup> in hexagonal NaYF<sub>4</sub> as compared to LiLuF<sub>4</sub> and LiYF<sub>4</sub>, making the former a more stable host material. This stability can also be provided when a core-shell combination of different materials is used, as heterogeneous combinations provide an interface that seem to hinder ion migration well. To the best of our knowledge this is the first time that such extensive studies on ion migration are performed on lanthanide doped LiLuF<sub>4</sub> nanoparticles. Considering these findings, it is strongly advised that for all new host materials a careful investigation in terms of ion migration, especially when used in complex core-shell-shell combinations, is carried out.

## Experimental Section

### *Synthesis*

All chemicals were commercially purchased and used without further purification if not indicated differently.

Synthesis of trifluoroacetate precursors for thermal decomposition synthesis.

$\text{RE}(\text{CF}_3\text{COO})_3$  with  $\text{RE}^{3+} = \text{Lu}, \text{Y}, \text{Yb}, \text{Er}$  were prepared according to the following protocol.<sup>33</sup> An appropriate amount of the corresponding oxides was placed in a 40 ml glass vial that was filled to one third with water and sonicated for 2 min in the ultrasound bath. After that the same volume of trifluoroacetic acid was added to the mixture under the fume hood. The mixture was placed in a sand bath set at 95 °C for at least 48 hours. The  $\text{CF}_3\text{COOLi}$  and  $\text{CF}_3\text{COONa}$  precursors were prepared using the same method, but  $\text{LiOH}$  or  $\text{Na}_2\text{CO}_3$  were taken instead of  $\text{Ln}_2\text{O}_3$ . After at least 48 h a powder was collected.

Synthesis of  $\text{LiREF}_4$  nanoparticles.

Thermal decomposition synthesis of undoped and 2%Er,18%Yb-doped  $\text{LiREF}_4$  nanoparticles.

The synthesis, adopted from Kaczmarek et al.<sup>20</sup> was as follows: 6 ml oleic acid, 2 ml 1-octadecene, 2 ml of oleylamine, 1 mmol of  $\text{CF}_3\text{COOLi}$  and 1 mmol of  $\text{RE}(\text{CF}_3\text{COO})_3$  (with  $\text{RE}^{3+} = 80\%\text{Lu}, 18\%\text{Yb}, 2\%\text{Er}; 100\%\text{Lu}$  or  $100\%\text{Er}$ ) were added to a three-neck glass flask. First the mixture was heated to 120 °C under vacuum and kept at this temperature for 30 min. After that initial step the atmosphere was changed to  $\text{N}_2$  gas flow, and the mixture was stirred at 120°C for 30 minutes. The last step was heating to 320 °C under nitrogen for 40 minutes. Next, the mixture was cooled down to room temperature. The washing steps were repeated three times and included precipitation with acetone, collecting by centrifuging, and redispersing in cyclohexane.

Co-precipitation synthesis of undoped and 2%Er,18%Yb:LiREF<sub>4</sub> nanoparticles and their consequent shells.

The synthesis for nanoparticles with LiLuF<sub>4</sub> or LiYbF<sub>4</sub> as host material for core and/or shell was adopted from Zhai et al.<sup>33</sup> The procedure was as follows: 4 ml oleic acid, 6 ml 1-octadecene and 1 mmol of RECl<sub>3</sub> (with RE<sup>3+</sup>= 80%Lu, 18%Yb, 2%Er or 100%Lu or 100%Yb) were set in a three-neck flask. This mixture was placed under vacuum at 120 °C for 2 hours in a Schlenk line until the chlorides were fully dissolved. If a shell was supposed to be grown, already prepared core nanoparticles had to be injected at this point of the synthesis. Consequently, the mixture was cooled down to 80°C under nitrogen flow and the previously prepared (2%Er,18%:)LiLuF<sub>4</sub> or LiErF<sub>4</sub> core NPs, prepared via thermal decomposition or co-precipitation, dispersed in 5 ml of cyclohexane were injected. After that the cyclohexane was evaporated under vacuum at 120 °C for 30 minutes. The following steps were necessary for core and shell alike: 2 mmol of NH<sub>4</sub>F and 1.5 mmol of LiOH were weighted off and separately dissolved in 2-3 ml of methanol in an ultrasound bath for at least 30 minutes. The mixture in the Schlenk line was cooled down to 50 °C under nitrogen flow. The dissolved NH<sub>4</sub>F and LiOH were quickly mixed and injected into the flask. For the nucleation step the flask was kept at 50 °C for 30 minutes after which the methanol was evaporated at 120 °C for 30 minutes under vacuum. The mixture was next heated to 310 °C and kept at constant temperature under nitrogen for 1 hour. In the last step the reaction was cooled down to room temperature. To purify the particles, they were precipitated in acetone, collected by centrifuging, and subsequently redispersed in cyclohexane, these steps were repeated three times.

The above described steps were also carried out for the 2%Er,18%Yb:LiYF<sub>4</sub> and undoped LiYF<sub>4</sub> core and shell synthesis with adjusted ratios of RECl<sub>3</sub> (with RE<sup>3+</sup>= 80%Y, 18%Yb, 2%Er or

100%Y) However, here the mixture of high boiling point solvent was different. Namely 7 ml oleic acid, 3 ml 1-octadecene for the core and 5 ml oleic acid, 5 ml 1-octadecene for the shell synthesis.

Synthesis of 2%Er,18%Yb:NaYF<sub>4</sub>@NaYF<sub>4</sub> nanoparticles.

Co-precipitation synthesis of 2%Er,18%Yb:NaYF<sub>4</sub>@NaYF<sub>4</sub> core-shell nanoparticles. The synthesis, adapted from Jena et al.<sup>34,12</sup> with some modifications was as follows: 3 ml oleic acid, 8.5 ml 1-octadecene and 0.5 mmol of RE(Ac)<sub>3</sub> (with RE<sup>3+</sup>= 80%Y, 18%Yb, 2%Er for the core and 100%Y for the shell), were placed in a three-neck flask, which was placed under vacuum at 120 °C for 30 minutes. If a shell was supposed to be grown around the previously made 2%Er,18%Yb:NaYF<sub>4</sub>, the reaction was cooled down to 80 °C under nitrogen flow and the pre-made core particles, dissolved in 5 ml of cyclohexane, were injected. The mixture was placed under vacuum again and heated to 120 °C for 30 minutes. The following steps were carried out for both core and shell synthesis: 2 mmol of NH<sub>4</sub>F and 1.25 mmol of NaOH were weighed off and separately dissolved in the ultrasound bath in 2-3 ml of methanol for 30 minutes. Afterwards, the mixture in the Schlenk line was cooled down to 50 °C under nitrogen and the dissolved NH<sub>4</sub>F and NaOH were mixed together and injected. The flask was kept at 50 °C for 30 minutes after which the methanol was evaporated at 120 °C for 30 minutes under vacuum. In the last step the reaction was heated to 300 °C and kept at this temperature for 110 minutes under nitrogen flow. The mixture was then cooled down to room temperature, precipitated in acetone, collected by centrifugation and redispersed in cyclohexane three times as described above.

Oleic acid ligand removal from nanoparticles.

Oleic acid ligand removal from the prepared nanoparticles was necessary to perform powder XRD and XRF measurements, as well as temperature-dependent photoluminescence measurements in the cryostat. For this purpose, the NPs, dispersed in 5 ml cyclohexane, were mixed with 10 ml of water to form two phases. 1M HCl solution was added until the pH value was 3 and the mixture was sonicated for 60 minutes. Afterwards the NPs were collected and washed with ethanol. If necessary, the whole procedure was repeated until the particles were well dispersible in water.

### *Characterization*

Transmission Electron Microscope (TEM) images were obtained with a JEOL JEM-2200FS TEM with Cs corrector, operated at 200 kV. Scanning TEM (STEM) images were taken with a high-angle annular dark field (HAADF) and bright field (BF) detector. STEM and EDX maps were performed via energy dispersive X-ray (EDX) spectroscopy in HAADF-STEM mode. Some TEM images in the supporting information (SI) were taken with a JEOL JEM1010 TEM without Cs correction, operated at 100 kV. All samples were prepared on a 300-mesh holey carbon copper grid, the NPs were applied via placing one or two drops of purified NPs dispersed in cyclohexane on the grid and drying it at room temperature afterwards. Photoluminescence (PL) spectra were recorded using an Edinburgh Instruments FLS920 UV-Vis-NIR spectrofluorometer that was equipped with a Hamamatsu R928P photomultiplier tube (PMT, Hamamatsu, Shizuoka, Japan). The excitation source was a power-tunable continuous wave (CW) laser (power limit:  $P_{\max} = 400$  mW, Livingston, UK) with an excitation wavelength of  $\lambda = 975$  nm. The samples were measured in a closed cycle cryostat (Advanced Research Systems, United States) at a temperature range between 280–480 K. The spectra were recorded in the range of  $\lambda = 500$ -750 nm. The step size and

dwelling time were kept the same. All thermometric calculations were performed using the *TeSen* software.<sup>25</sup> Decay times were measured on the same setup generating a pulsed signal from the 975 nm CW laser. Powder X-ray diffraction (PXRD) patterns were collected on a Bruker D8 Advance diffractometer equipped with an autochanger and LynxEye XE-T Silicon strip Line detector, operated at 40 kV, 30 mA using Cu-K $\alpha$  radiation ( $\lambda = 1.5406 \text{ \AA}$ ) in a Bragg-Brentano geometry. Energy Dispersive X-Ray Fluorescence (XRF) was performed with a Rigaku NEX CG Spectrometer in powder form. The Rigaku NEX CG works with a close-coupled Cartesian Geometry under helium flow and is equipped with a Pd anode X-ray tube and a silicon drift detector.

## ASSOCIATED CONTENT

The Supporting Information is available free of charge at: xxx

Additional TEM and STEM images as well as EDX maps, PXRD patterns, histograms of nanoparticle size distribution, additional photoluminescence data and decay time studies, XRF spectra.

## AUTHOR INFORMATION

### Author Contributions

The manuscript was written through contributions of all authors. All authors have given approval to the final version of the manuscript.

### Funding Sources

These results are part of a project that has received funding from the European Research Council (ERC) under the European Union's Horizon 2020 research and innovation programme (Grant agreement No. 945945).

#### ACKNOWLEDGMENT

H.R. acknowledges support and funding as postdoctoral fellow fundamental research of the Research Foundation - Flanders (FWO) under grant number 1273621N. The authors thank Laurens Bourda for help with some of the PXRD measurements.

#### REFERENCES

- (1) Fu H., Ma Y., Liu Y. and Hong M. Local-structure-dependent luminescence in lanthanide-doped inorganic nanocrystals for biological applications. *Chem. Commun.*, **2021**, 57, 2970–2981.
- (2) Ansari A.A., Parchur A.K., Nazeeruddin M. and Tavakoli M.M. Luminescent lanthanide nanocomposites in thermometry: Chemistry of dopant ions and host matrices. *Coord. Chem. Rev.*, **2021**, 444, 214040.
- (3) Yang Y., Tu D., Zhang Y., Zhang P. and Chen X. Recent advances in design of lanthanide-containing NIR-II luminescent nanoprobe. *Iscience*, **2021**, 24, 102062.
- (4) Chen G., Qiu H., Prasad P. N. and Chen X. Upconversion nanoparticles: design, nanochemistry, and applications in theranostics. *Chem. Rev.*, **2014**, 114, 5161–5214.
- (5) Dramicanin M., *Luminescence thermometry: methods, materials, and applications*, Woodhead Publishing, **2018**.

- (6) Bednarkiewicz A., Marciniak L., Carlos L. D. and Jaque D. Standardizing luminescence nanothermometry for biomedical applications. *Nanoscale*, **2020**, 12, 14405–14421.
- (7) Dong H., Sun L. D. and Yan C.H. Versatile spectral and lifetime multiplexing nanoplatfrom with excitation orthogonalized upconversion luminescence. *ACS Nano*, **2017**, 44, 1608–1634.
- (8) Liu J., Rijckaert H., Zeng M., Haustraete K., Laforce B., Vincze L., Van Driessche I., Kaczmarek A. M. and Van Deun R. Simultaneously excited downshifting/upconversion luminescence from lanthanide-doped core/shell fluoride nanoparticles for multimode anticounterfeiting. *Adv. Funct. Mat.*, **2018**, 28, 1707365.
- (9) Kim S. Y., Won Y. H. and Jang H. S. A Strategy to enhance  $\text{Eu}^{3+}$  emission from  $\text{LiYF}_4:\text{Eu}$  nanophosphors and green-to-orange multicolor tunable, transparent nanophosphor-polymer composites. *Sci. Rep.*, **2015**, 5(1), 1-11, 7866.
- (10) Wang Y. The role of an inert shell in improving energy utilization in lanthanide-doped upconversion nanoparticles. *Nanoscale*, **2019**, 11, 10852–10858.
- (11) Lo W. S., Wong W. T. and Law G. L. Friend or foe? The role of solvents in non-triplet, intraligand charge transfer sensitization of lanthanide (III) luminescence. *RSC Adv.*, **2016**, 6, 74100–74109.
- (12) Rabouw F. T., Prins P. T., Villanueva-Delgado P., Castelijns M., Geitenbeek R. G. and Meijerink A. Quenching pathways in  $\text{NaYF}_4:\text{Er}^{3+}, \text{Yb}^{3+}$  upconversion nanocrystals., *ACS Nano*, **2018**, 12, 4812–4823.
- (13) Ferreira F. d. S., de Moraes A. J., Santos Calado C. M., Iikawa F., Couto Junior O. D. D., Brunet G., Murugesu M., Mazali I. O. and Sigoli F. A. Dual magnetic field and temperature optical

probes of controlled crystalline phases in lanthanide-doped multi-shell nanoparticles. *Nanoscale*, **2021**, 13(35), 14723-14733.

(14) Sun, T., Chen, B., Guo, Y., Zhu, Q., Zhao, J., Li, Y., Wang, F. Ultralarge anti-Stokes lasing through tandem upconversion. *Nat. Commun.*, **2022**. 13(1), 1-7.

(15) Abel K. A., Boyer J. C., Andrei C. M., van Veggel F. C. J. M. Analysis of the Shell Thickness Distribution on NaYF<sub>4</sub>/NaGdF<sub>4</sub> Core/Shell Nanocrystals by EELS and EDS. *JPC Letters*, **2011**, 2, 185

(16) Hudry D., Busko D., Popescu R., Gerthsen D., Abeykoon A. M. M., Kübel C., Bergfeldt T., Richards B. S. Direct evidence of significant cation intermixing in upconverting core@ shell nanocrystals: Toward a new crystallochemical model. *J. Mater. Chem.*, **2017**, 29, 9238

(17) Hudry D., Popescu R., Busko D., Diaz-Lopez M., Abeykoon M., Bordet P., Gerthsen D., Howard I. A., Richards B. S. Interface disorder in large single-and multi-shell upconverting nanocrystals. *J. Mater. Chem. C*, **2019**, 7, 1164.

(18) Xu X., Clarke C., Ma C., Casillas G., Das M., Guan M., Liu D., Wang L., Tadich A., Du Y., Ton-That C., Jin D. Depth-profiling of Yb<sup>3+</sup> sensitizer ions in NaYF<sub>4</sub> upconversion nanoparticles. *Nanoscale*, **2017**, 9, 7719.

(19) Shin J., Kyhm J. H., Hong A. R., Song J. D., Lee K., Ko H. and Jang H. S. Multicolor tunable upconversion luminescence from sensitized seed-mediated grown LiGdF<sub>4</sub>:Yb,Tm-based core/triple-shell nanophosphors for transparent displays. *J. Mater. Chem.*, **2018**, 30, 8457–8464

- (20) Kaczmarek A. M., Suta M., Rijckaert H., van Swieten T. P., Van Driessche I., Kaczmarek M. K. and Meijerink A. High temperature (nano) thermometers based on  $\text{LiLuF}_4:\text{Er}^{3+},\text{Yb}^{3+}$  nano- and microcrystals. *J. Mater. Chem. C*, **2021**, 9, 3589–3600.
- (21) Dalpian G. M. and Chelikowsky J. R. Self-purification in semiconductor nanocrystals. *Phys. Rev. Lett.*, **2006**, 96, 226802.
- (22) Huang P., Zheng W., Zhou S., Tu D., Chen Z., Zhu H., Li R., Ma E., Huang M. and Chen X. Lanthanide-doped  $\text{LiLuF}_4$  upconversion nanoprobles for the detection of disease biomarkers. *Angew. Chem.*, **2014**, 126, 1276–1281.
- (23) Goryunov A. and Popov A. Crystal Structure of Lithium and Yttrium coiapt. with fluorides. *J. Chem.*, **1992**, 37(2), 276-279.
- (24) Dong Y. M., Xia H. P., Fu L., Li S. S., Gu X. M., Zhang J. L., Wang D. J., Zhang Y. P., Jiang H. C. and Chen B. J. White light emission from  $\text{Dy}^{3+}$ -doped  $\text{LiLuF}_4$  single crystal grown by Bridgman method. *Optoelectron. Lett.*, **2014**, 10, 262–265.
- (25) Kaczmarek A. M., Van Deun R. and Kaczmarek M. K. *TeSen*–tool for determining thermometric parameters in ratiometric optical thermometry. *Sens. Actuators B: Chem.*, **2018**, 273, 696–702. 21
- (26) Semashko V., Korableva S., Nizamutdinov A., Kuznetsov S., Pynenkov A., Popov P., Baranchikov A., Nishchev K., Ivanov V. and Fedorov P. Phase Equilibria in  $\text{LiYF}_4\text{--LiLuF}_4$  System and Heat Conductivity of  $\text{LiY}_{1-x}\text{Lu}_x\text{F}_4$  Single Crystals. *Russ. J. Inorg. Chem.*, **2018**, 63, 433–438.

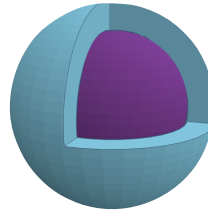
- (27) Huang P., Zheng W., Tu D., Shang X., Zhang M., Li R., Xu J., Liu Y. and Chen X. Unraveling the electronic structures of neodymium in LiLuF<sub>4</sub> nanocrystals for ratiometric temperature sensing. *Adv. Sci.*, **2019**, 6, 1802282.
- (28) Grzechnik A., Friese K., Dmitriev V., Weber H. P., Gesland J. Y. and Crichton W. A. Pressure-induced tricritical phase transition from the scheelite structure to the fergusonite structure in LiLuF<sub>4</sub>. *J. Phys. Condens. Matt.*, **2005**, 17, 763.
- (29) Shi R., Martinez E. D., Brites C. D. and Carlos L. D. Thermal enhancement of upconversion emission in nanocrystals: a comprehensive summary. *PCCP*, **2021**, 23, 20–42.
- (30) Zhu Y., Zhao S., Zhou B., Zhu H., Wang Y. Enhancing upconversion luminescence of LiYF<sub>4</sub>:Yb,Er nanocrystals by Cd<sup>2+</sup> doping and core–shell structure. *J. Phys. Chem. C*, **2017**, 121(34), 18909-18916.
- (31) Dong H., Sun L. D., Yan C. H. Local structure engineering in lanthanide-doped nanocrystals for tunable upconversion emissions. *JACS*, **2021**, 143(49), 20546-20561.
- (32) Dong C., Pichaandi J., Regier T., van Veggel F. C. The unexpected structures of “core–shell” and “alloy” LnF<sub>3</sub> nanoparticles as examined by variable energy X-ray photo-electron spectroscopy. *Nanoscale*, **2011**, 3(8), 3376-3384.
- (33) Zhai X., Lei P., Zhang P., Wang Z., Song S., Xu X., Liu X., Feng J. and Zhang H. Growth of lanthanide-doped LiGdF<sub>4</sub> nanoparticles induced by LiLuF<sub>4</sub> core as tri-modal imaging bioprobes. *Biomaterials*, **2015**, 65, 115–123.

(34) Jena H. S., Rijckaert H., Krishnaraj C., and Kaczmarek A. M. Hybrid Nanocomposites Formed by Lanthanide Nanoparticles in Zr-MOF for Local Temperature Measurements during Catalytic Reactions. *Chem. Mat.*, **2021**, 33(20), 8007-8017.



Er,Yb:LiLuF<sub>4</sub>

Suppressed  
ion migration  
→



Er,Yb:LiLuF<sub>4</sub>@  
LiYF<sub>4</sub>

